

# Cooperative effect between copper species and oxygen vacancy in $\text{Ce}_{0.7-x}\text{Zr}_x\text{Cu}_{0.3}\text{O}_2$ catalysts for carbon monoxide oxidation

Shan Wang<sup>1,2</sup>, Xuelian Xu<sup>2</sup>, Ping Xiao<sup>2</sup>, Junjiang Zhu (✉)<sup>2</sup>, Xinying Liu (✉)<sup>1</sup>

<sup>1</sup> Institute for the Development of Energy for African Sustainability, College of Science, Engineering and Technology, University of South Africa, Johannesburg 1710, South Africa

<sup>2</sup> Hubei Key Laboratory of Biomass Fibers and Eco-dyeing & Finishing, College of Chemistry and Chemical Engineering, Wuhan Textile University, Wuhan 430200, China

© Higher Education Press 2021

**Abstract** The effects of Zr doping on the existence of Cu and the catalytic performance of  $\text{Ce}_{0.7-x}\text{Zr}_x\text{Cu}_{0.3}\text{O}_2$  for CO oxidation were investigated. The characterization results showed that all samples have a cubic structure, and a small amount of Zr doping facilitates  $\text{Cu}^{2+}$  ions entering the  $\text{CeO}_2$  lattice, but excessive Zr doping leads to the formation of surface CuO crystals again. Thus, the number of oxygen vacancies caused by the  $\text{Cu}^{2+}$  entering the lattice (e.g.,  $\text{Cu}^{2+}-\square-\text{Ce}^{4+}$ ;  $\square$ : oxygen vacancy), and the amount of reducible copper species caused by CuO crystals, varies with the Zr doping. Catalytic CO oxidation tests indicated that the oxygen vacancy and the reducible copper species were the adsorption and activation sites of  $\text{O}_2$  and CO, respectively, and the cooperative effects between them accounted for the high CO oxidation activity. Thus, the samples  $x = 0.1$  and  $0.3$ , which possessed the most oxygen vacancy or reducible copper species, showed the best activity for CO oxidation, with full CO conversion obtained at  $110^\circ\text{C}$ . The catalyst is also stable and has good resistance to water during the reaction.

**Keywords** Ce–Zr–Cu–O, CO oxidation, reducible copper species, oxygen vacancy, cooperative effect

## 1 Introduction

Air pollution causes serious damage to people's health. CO is a major component of air pollution, and its elimination at a low temperature is an important research issue [1–3]. In

the past few decades, the catalytic oxidation technique has been widely used to control CO emitted from industrial sources, with great success [4,5]. Hence, the development of active catalysts for CO oxidation is an important issue in the industry, and continues to attract the attention of researchers [6,7].

Precious metals are efficient for low-temperature CO oxidation reaction [8–10], but the high cost and scarcity limit large-scale application [11]. Therefore, attention has been given to the non-precious metal catalysts in recent years, including Ce–Zr–Cu mixed metal oxides, which are low-cost, and have strong sintering resistance and good low-temperature activity [12,13].

CuO is low-cost and shows good low-temperature activity for CO oxidation, but its activity is affected in the presence of  $\text{H}_2\text{O}$  and  $\text{CO}_2$  [14,15].  $\text{CeO}_2$  is an important catalytic material widely used in applications such as three-way catalysts to purify automobile exhaust fumes [16,17], owing to its strong reducibility, stability and good oxygen storage/release capacity [18,19]. Therefore,  $\text{CeO}_2$  is widely used as a support or promoter of catalysts [20], and it was also reported that  $\text{CeO}_2$  can promote the dispersion of Cu species and increase the storage of oxygen species [21].

Recent reports indicate that the synergistic effect between CuO and  $\text{CeO}_2$  can improve the oxidation-reduction ability of the CuO/ $\text{CeO}_2$  catalyst [22], and thus exhibit good activity for low-temperature CO oxidation [23]. In addition, it has been found that the thermal stability, redox activity and catalytic performance of  $\text{CeO}_2$  can be improved by replacing part of the Ce atoms with Zr or La atoms in the lattice [24,25]. Although  $\text{ZrO}_2$  cannot catalyze the reaction itself, it can interact with  $\text{CeO}_2$  and form a Ce(Zr) $\text{O}_2$  solid solution, which promotes the

oxygen storage/release capacity and redox properties of  $\text{CeO}_2$ , and thus the low-temperature oxidation activity [26,27]. It was also reported that the excellent performance of  $\text{CeO}_2$  was mainly caused by oxygen vacancy [28], and that the incorporation of ions with suitable radii and valences (e.g.,  $\text{Cu}^{2+}$ ) facilitated the production of oxygen vacancy [29].

Qi et al. [30] studied the effects of cerium precursors (e.g.,  $\text{Ce}(\text{NO}_3)_3$  and  $(\text{NH}_4)_2\text{Ce}(\text{NO}_3)_6$ ) on the structure, surface state, reducibility and CO oxidation activity of mesoporous  $\text{CuO-CeO}_2$ . They found that surface  $\text{Cu}^+$  was the active site of CO, and the synergistic effects between Cu and Ce facilitated the catalytic activity of  $\text{CuO-CeO}_2$ . Cecilia et al. [31] synthesized  $\text{CuO-Ce}_{0.9}\text{X}_{0.1}\text{O}_2$  catalysts for CO preferential oxidation ( $\text{H}_2$ ), and showed that  $\text{CuO-Ce}_{0.9}\text{Zr}_{0.1}\text{O}_2$  was the most active catalyst for the reaction, with 95% CO conversion obtained at 120 °C. Carmona et al. [32] prepared  $\text{CuO-CeO}_2$  catalysts supported on Zr-doped SBA-15 for CO preferential oxidation, and found that the CO conversion was improved, owing to the improved dispersion and reducibility of Cu species caused by Zr doping [18].

In this study, a series of  $\text{Ce}_{0.7-x}\text{Zr}_x\text{Cu}_{0.3}\text{O}_2$  catalysts were prepared using a sol-gel method, and the effect of Zr doping on their physicochemical properties and catalytic activity for CO oxidation were studied. The aim of this work was to study how Zr doping affects the structural features and the catalytic performance of  $\text{Ce}_{0.7-x}\text{Zr}_x\text{Cu}_{0.3}\text{O}_2$  for CO oxidation. To illustrate this point, a series of measurements were used to characterize the catalysts (including X-ray diffraction (XRD),  $\text{N}_2$  physisorption, transmission electron microscopy (TEM), scanning electron microscopic (SEM),  $\text{O}_2$ -temperature programmed desorption ( $\text{O}_2$ -TPD),  $\text{H}_2$ -temperature programmed reduction ( $\text{H}_2$ -TPR) and X-ray photoelectron spectroscopy (XPS)), and the results were correlated to the CO oxidation activity. Finally, the reaction stability and the water resistance of  $\text{Ce}_{0.4}\text{Zr}_{0.3}\text{Cu}_{0.3}\text{O}_2$  (the best catalyst for CO oxidation) were also investigated, to evaluate the potential for industrial applications.

## 2 Experimental

### 2.1 Catalyst preparation

The  $\text{Ce}_{0.7-x}\text{Zr}_x\text{Cu}_{0.3}\text{O}_2$  catalysts were prepared using a sol-gel method. First, 0.1 g F127, 2.1 g citric acid, and  $\text{Ce}(\text{NO}_3)_3/\text{ZrO}(\text{NO}_3)_2/\text{Cu}(\text{NO}_3)_2$ , with expected molar ratios (0.02 moles in total), were added to 10 g ethanol solution (40%), which was stirred until completely dissolved. The solution was continuously stirred until it gelatinized. The gel was dried at 100 °C for 8 h, calcined at 300 °C for 3 h and at 500 °C for 5 h (heating rate: 1 °C·min<sup>-1</sup>). The product was denoted  $\text{Ce}_{0.7-x}\text{Zr}_x\text{Cu}_{0.3}\text{O}_2$  ( $x = 0, 0.1, 0.3, 0.5$ ). For comparison purposes, the

monomer  $\text{CeO}_2$  and  $\text{CuO}$  catalysts were prepared using the same procedure.

### 2.2 Catalyst characterization

XRD patterns were recorded on an Advance IIIX-type apparatus (Bruker, Germany) using  $\text{Cu K}\alpha$  radiation, and operating at 40 kV and 30 mA. The samples were scanned at  $2\theta$  range of 10°–80° and a scanning speed of 0.2°·s<sup>-1</sup>. XPS was recorded on a VG Multilab 2000 apparatus (Thermo Scientific) equipped with an amonochromated Al  $\text{K}\alpha$  X-ray source. The binding energy was calibrated using the C 1s of adventitious carbon at 284.8 eV. Peak deconvolution was performed using XPSPEAK software.  $\text{N}_2$  physisorption isotherms were measured on a BeiShiDe 3H-2000PS2 apparatus at -196 °C, and the surface area was calculated by multiple points using the Brunauer-Emmett-Teller (BET) method. Before measurement, the samples were vacuumed at 300 °C for 3 h. SEM images were obtained using a JSM-IT500A electron microscope (JEOL, Japan). TEM was performed on a Tecnai G2 F20 instrument equipped with a field emission gun operated at 200 kV.

$\text{O}_2$ -TPD and  $\text{H}_2$ -TPR profiles were obtained using a TP-5080 TPD/TPR instrument made by Tianjin Xianquan Company. For  $\text{O}_2$ -TPD, 0.10 g catalysts were treated at 500 °C for 1 h in an oxygen atmosphere. After cooling to room temperature, the oxygen was replaced with Ar at a flow rate of 20 mL·min<sup>-1</sup>. When the baseline was stable, the temperature was increased from 50 °C to 900 °C at a rate of 10 °C·min<sup>-1</sup>. For  $\text{H}_2$ -TPR, 0.03 g catalysts were pre-treated in Ar at 500 °C for 1 h and then cooled to 50 °C. The flow gas was then switched to 5%  $\text{H}_2/\text{N}_2$  (20 mL·min<sup>-1</sup>). After a stable baseline was reached, the sample was heated from 50 °C to 800 °C at a rate of 10 °C·min<sup>-1</sup>.

### 2.3 Catalytic activity tests

The CO oxidation reaction was performed on a fixed-bed quartz micro-reactor (i.d. = 6 mm). The catalyst (0.15 g) was loaded into a micro-reactor without dilution. The reactant (0.8 vol-% CO + 6.0 vol-%  $\text{O}_2$ , balanced with Ar) was passed at a flow rate of 60 mL·min<sup>-1</sup>, with the weight hourly space velocity (WHSV) equating to 31000 h<sup>-1</sup>. The reaction temperature was controlled by a temperature programming computer. At each stage, the temperature was maintained for 30 min before testing the reaction activity, to ensure that the reaction had reached steady-state. The activity was evaluated in terms of CO conversion:

$$\% \text{CO conversion} = ([\text{CO}]_{\text{in}} - [\text{CO}]_{\text{out}}) / [\text{CO}]_{\text{in}} \times 100,$$

where  $[\text{CO}]_{\text{in}}$  and  $[\text{CO}]_{\text{out}}$  are the inlet and outlet CO concentrations, respectively.

### 3 Results and discussion

#### 3.1 Textural properties and surface morphologies

Figure 1 shows the XRD patterns of the catalysts. The  $\text{CeO}_2$  and  $\text{CuO}$  formed well-crystallized cubic fluorite  $\text{CeO}_2$  (PDF #34-0394) and monoclinic  $\text{CuO}$  (PDF #48-1548) structures. The  $\text{Ce}_{0.7}\text{Cu}_{0.3}\text{O}_2$  sample showed mainly the diffraction peaks of  $\text{CeO}_2$ , but some weak diffraction peaks also appeared ( $2\theta = 35.6^\circ, 38.8^\circ$ ), which can be assigned to  $\text{CuO}$ . This suggests that the  $\text{Cu}^{2+}$  ions did not enter the  $\text{CeO}_2$  lattice fully and some formed on the surface as  $\text{CuO}$  crystals. The entrance of  $\text{Cu}^{2+}$  ions to the  $\text{CeO}_2$  lattice was verified by the peak shift of  $\text{CeO}_2$  from  $28.47^\circ$  to  $28.59^\circ$  (Fig. 1(a)). From the Scherrer equation ( $2d\sin\theta = n\lambda$ ), we know that the lattice distance of  $\text{CeO}_2$  will shrink when  $\text{Cu}^{2+}$  with a smaller ionic radius ( $r_{\text{Cu}^{2+}} = 73 \text{ \AA}$ ,  $r_{\text{Ce}^{4+}} = 87 \text{ \AA}$ ) enters the lattice, causing the shift of diffraction peaks to a higher position. Moreover, according to the principle of electroneutrality, the substitution of  $\text{Ce}^{4+}$  with low valence  $\text{Cu}^{2+}$  will lead to the generation of oxygen vacancy in the  $\text{CeO}_2$  structure (e.g.,  $\text{Cu}^{2+} - \square - \text{Ce}^{4+}$ ;  $\square$ : oxygen vacancy), and facilitate the CO oxidation reaction.

Zr doping influenced the formation of  $\text{CuO}$  on the surface. With  $\text{Ce}_{0.6}\text{Zr}_{0.1}\text{Cu}_{0.3}\text{O}_2$ , the diffraction peak of  $\text{CuO}$  was hard to observe in the XRD pattern (Fig. 1(b)). This indicates that Zr doping in small amounts can promote  $\text{Cu}^{2+}$  ions entering the  $\text{CeO}_2$  lattice. However, with a further increase in Zr doping ( $x > 0.1$ ), the diffraction peaks of  $\text{CuO}$  appeared and strengthened, which indicates that excessive Zr doping causes the segregation of  $\text{CuO}$  on the surface. It is likely that, at low levels of  $\text{Zr}^{4+}$  doping, the defects of  $\text{CeO}_2$  caused by  $\text{Ce}^{3+}$  (see the XPS spectra below) were mostly repaired by replacing  $\text{Ce}^{3+}$  with  $\text{Zr}^{4+}$ , which allows more  $\text{Cu}^{2+}$  ions to enter the  $\text{CeO}_2$  lattice. However, because of the different

ionic radii between  $\text{Ce}^{4+}$  and  $\text{Zr}^{4+}$ , the further increase in  $\text{Zr}^{4+}$  doping causes lattice distortion of  $\text{CeO}_2$ , which decreases the accommodation capability of  $\text{Ce}(\text{Zr})\text{O}_2$  to  $\text{Cu}^{2+}$  ions; this leads to the re-formation of surface  $\text{CuO}$ .

Although the cubic structure was kept even at Zr doping of 50% (i.e.,  $\text{Ce}_{0.2}\text{Zr}_{0.5}\text{Cu}_{0.3}\text{O}_2$ ), the diffraction peaks shifted significantly to a higher position (e.g., from  $28.8^\circ$  to  $29.5^\circ$ ). This indicates that the matrix structure of the catalyst was gradually transferred to cubic  $\text{ZrO}_2$  (PDF #49-1642), see Fig. 1(b). This demonstrates that the  $\text{Zr}^{4+}$  ions entered the  $\text{CeO}_2$  lattice and formed a  $\text{Ce}(\text{Zr})\text{O}_2$  solid solution. In contrast, the number of  $\text{Cu}^{2+}$  ions entering the  $\text{CeO}_2$  lattice is limited, due to its low oxidation state (+2), compared to that of  $\text{Ce}^{4+}$  and  $\text{Zr}^{4+}$  ions (+4).

To confirm the actual Zr and Cu atoms doped to the  $\text{CeO}_2$  lattice, inductively coupled plasma mass spectrometer measurements were conducted (The results are listed in Table S1, cf. Electronic Supplementary Material, ESM). Table S1 shows that the Ce/Zr/Cu molar ratios of  $\text{Ce}_{0.7}\text{Cu}_{0.3}\text{O}_2$ ,  $\text{Ce}_{0.6}\text{Zr}_{0.1}\text{Cu}_{0.3}\text{O}_2$  and  $\text{Ce}_{0.4}\text{Zr}_{0.3}\text{Cu}_{0.3}\text{O}_2$  accord well with their nominal compositions, which demonstrates that the Zr and Cu atoms were doped as desired.

$\text{N}_2$  physisorption isotherms showed that all samples have the type III isotherm with a H4 hysteresis loop (Fig. 2), which suggests the presence of interstitial holes created between the particles. The change in the BET surface area after Zr doping is complex, and could be related to the formation of surface  $\text{CuO}$  crystals. Thus, the increase in surface area from  $\text{Ce}_{0.7}\text{Cu}_{0.3}\text{O}_2$  to  $\text{Ce}_{0.6}\text{Zr}_{0.1}\text{Cu}_{0.3}\text{O}_2$  was the largest of the Cu species that entered the  $\text{Ce}(\text{Zr})\text{O}_2$  lattice, which decreased the number of particles on the surface and hence exposed more pores. The  $\text{CuO}$  crystal formed again from  $\text{Ce}_{0.6}\text{Zr}_{0.1}\text{Cu}_{0.3}\text{O}_2$  to  $\text{Ce}_{0.4}\text{Zr}_{0.3}\text{Cu}_{0.3}\text{O}_2$ , and filled in or blocked the holes made between the  $\text{Ce}(\text{Zr})\text{O}_2$  particles, thus decreasing the surface area. With a further increase in Zr doping, i.e.,

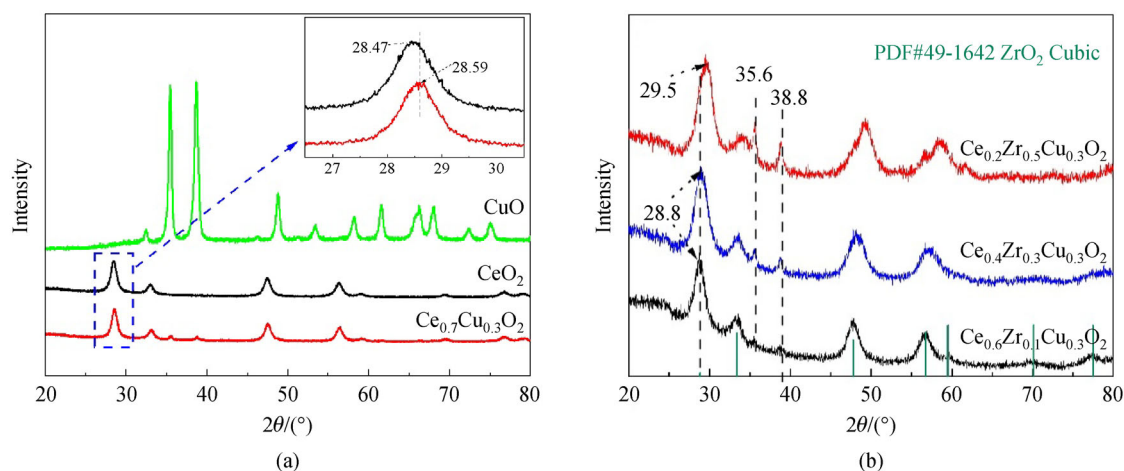


**Fig. 1** XRD patterns for: (a) individual  $\text{CuO}$ ,  $\text{CeO}_2$  and  $\text{Ce}_{0.7}\text{Cu}_{0.3}\text{O}_2$  composites and (b) the Zr doped  $\text{Ce}_{0.7-x}\text{Zr}_x\text{Cu}_{0.3}\text{O}_2$  composites, together with a standard diffraction diagram of the cubic  $\text{ZrO}_2$ .

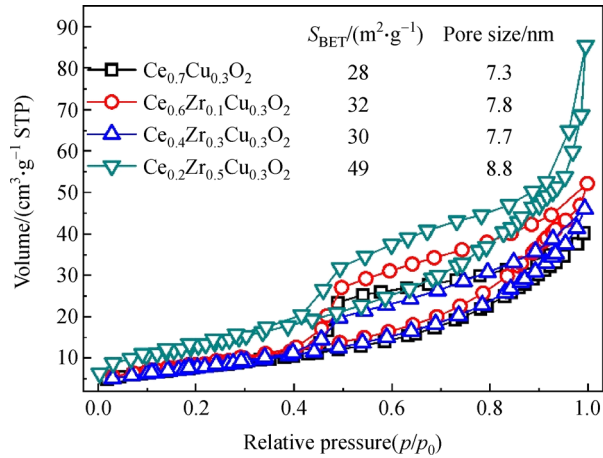


**Fig. 2**  $N_2$  physisorption isotherms of the  $Ce_{0.7-x}Zr_xCu_{0.3}O_2$ , with BET surface area and pore size data inserted.

from  $Ce_{0.4}Zr_{0.3}Cu_{0.3}O_2$  to  $Ce_{0.2}Zr_{0.5}Cu_{0.3}O_2$ , the matrix structure gradually transformed to that of  $ZrO_2$ , and altered the textural properties and the surface area. It was reported that Zr doping can improve the surface area of  $CeO_2$  [33], thus it can be expected that the surface area increases (from 30 to  $49 \text{ m}^2 \cdot \text{g}^{-1}$ ) when the matrix structure is transformed from  $CeO_2$  to  $ZrO_2$ .

Figure 3 presents the SEM images of  $Ce_{0.7-x}Zr_xCu_{0.3}O_2$ , showing a random surface morphology with a wide range of particle sizes. The morphology of

$Ce_{0.6}Zr_{0.1}Cu_{0.3}O_2$  varied greatly compared to that of the other samples, in that it has a looser and rougher surface, while the other samples have a more densely packed and smoother surface. This could be attributed to the formation of CuO crystals on the surface. For  $Ce_{0.6}Zr_{0.1}Cu_{0.3}O_2$  with few surface CuO crystals, most of the Cu species enters the  $Ce(Zr)O_2$  lattice and shows mainly the surface morphology of  $Ce(Zr)O_2$ , which has good resistance to sintering. The other samples that showed many surface CuO crystals (which tend to agglomerate at high temperature) were sintered during the calcination process and the surface became smooth. This result can be seen as indirect evidence that most of the Cu species of  $Ce_{0.6}Zr_{0.1}Cu_{0.3}O_2$  entered the  $Ce(Zr)O_2$  lattice, instead of forming CuO crystals on the surface.

TEM measurements were conducted to further observe the surface morphology of the samples (Figs. 4(a–c)). For  $Ce_{0.7}Cu_{0.3}O_2$  without Zr doping, a large number of small particles ( $\sim 8 \text{ nm}$ ) were observed on the surface, which can be attributed to the surface CuO crystals. The number of particles on the surface decreased significantly when a small amount of Zr was doped (i.e.,  $Ce_{0.4}Zr_{0.3}Cu_{0.3}O_2$ ), with the Cu species seen in both the  $Ce(Zr)O_2$  lattice and on the surface. However, a further increase in Zr doping (i.e.,  $Ce_{0.2}Zr_{0.5}Cu_{0.3}O_2$ ) led to more particles forming on the surface, and the particle size varied widely (from 5.0 to 18.1 nm), due to the transfer of the matrix structure. This accords well with the changes observed in the XRD patterns, which showed that the CuO crystals disappeared

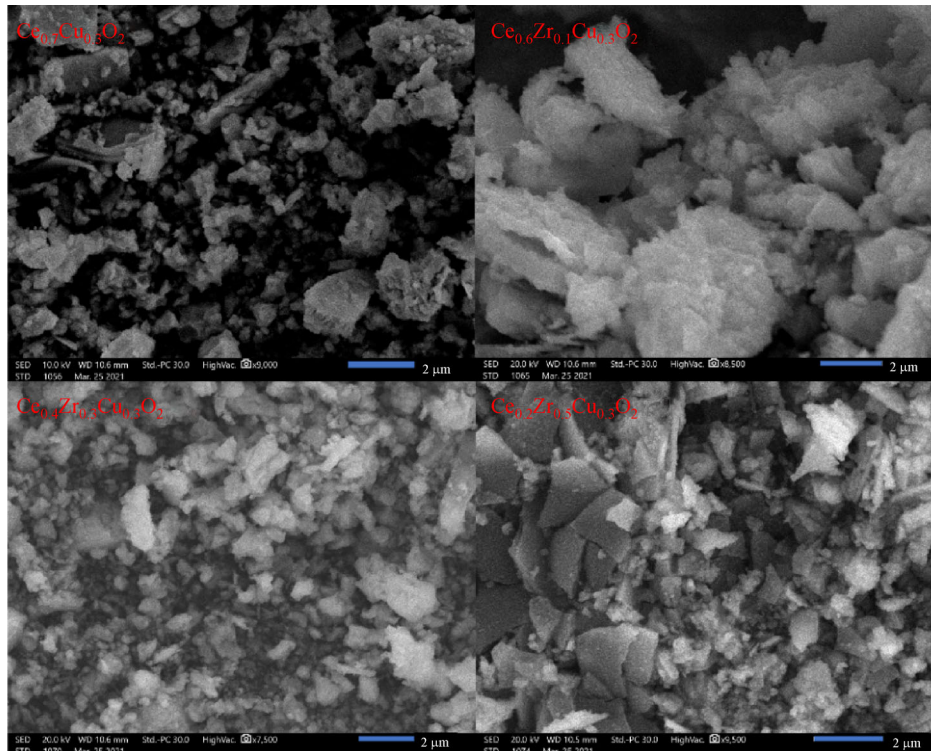


**Fig. 3** SEM images of the  $Ce_{0.7-x}Zr_xCu_{0.3}O_2$  series samples.

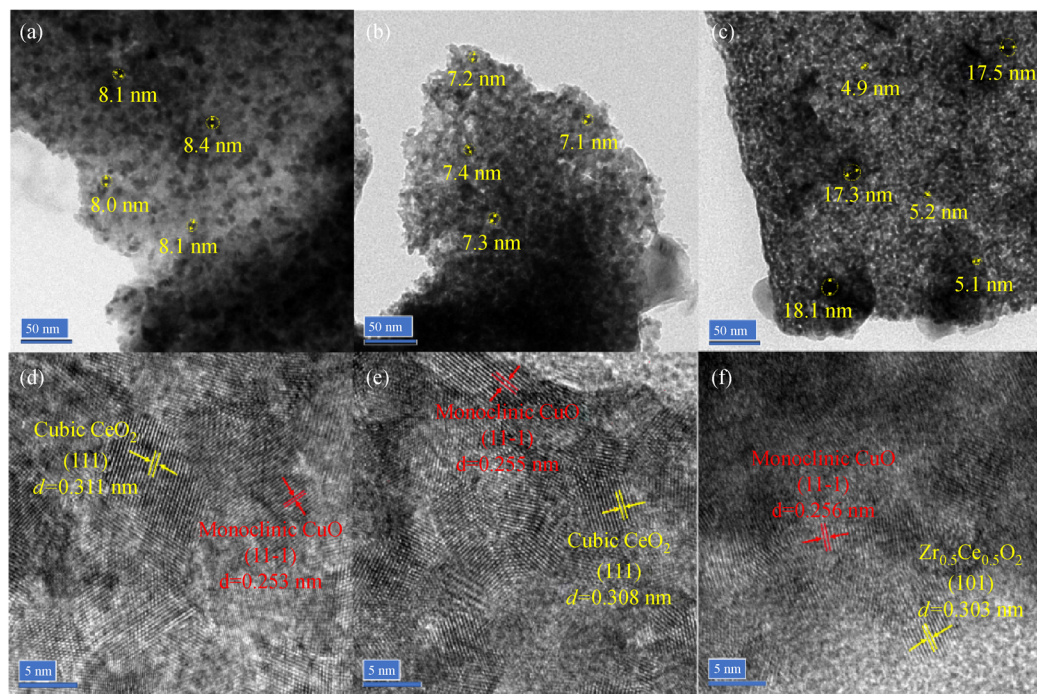


**Fig. 4** Normal (a–c) and high (d–f) resolution TEM images of:  $\text{Ce}_{0.7}\text{Cu}_{0.3}\text{O}_2$  (a, d),  $\text{Ce}_{0.4}\text{Zr}_{0.3}\text{Cu}_{0.3}\text{O}_2$  (b, e), and  $\text{Ce}_{0.2}\text{Zr}_{0.5}\text{Cu}_{0.3}\text{O}_2$  (c, f).

initially, but re-appeared with a further increase in Zr doping.

The high resolution transmission electron microscope pictures supported the above results, i.e., the Cu species entered the Ce(Zr)O<sub>2</sub> lattice at Zr doping  $\leq 30\%$ , and the matrix structure was transferred at Zr doping of 50% (Figs. 4(d–e)). Both  $\text{Ce}_{0.7}\text{Cu}_{0.3}\text{O}_2$  and  $\text{Ce}_{0.4}\text{Zr}_{0.3}\text{Cu}_{0.3}\text{O}_2$  showed a lattice distance of  $\sim 0.309$  nm, which can be assigned to the  $d_{(111)}$  of CeO<sub>2</sub> (0.312 nm, PDF #43-1002). The slight decrease in the  $d_{(111)}$  value suggests that Cu<sup>2+</sup> or Zr<sup>4+</sup> with a smaller ionic radius entered the CeO<sub>2</sub> lattice. Additionally, a lattice distance of  $\sim 0.254$  nm was also observed for the two samples, which can be assigned to the  $d_{(11-1)}$  of monoclinic CuO (0.252 nm, PDF #48-1548), since CuO crystals are present on the surface. With  $\text{Ce}_{0.2}\text{Zr}_{0.5}\text{Cu}_{0.3}\text{O}_2$ , the (111) lattice fringe of CeO<sub>2</sub> was not observed, but it appeared with a lattice distance of 0.303 nm, which can be assigned to the  $d_{(101)}$  of the Ce–Zr–O solid solution [34]. This, in turn, confirms the transformation of the matrix structure from CeO<sub>2</sub> to ZrO<sub>2</sub>. As expected, a lattice distance of 0.256 nm (assigned to the  $d_{(11-1)}$  of monoclinic CuO) was observed, due to the re-formation of surface CuO.

### 3.2 Redox and surface properties

The H<sub>2</sub>-TPR profiles of  $\text{Ce}_{0.7-x}\text{Zr}_x\text{Cu}_{0.3}\text{O}_2$  are depicted in Fig. 5. They show two reduction peaks for all samples, with a shoulder peak at 130 °C–200 °C and a main peak at 200 °C–270 °C. The former can be assigned to the reduction of highly dispersed CuO particles having strong

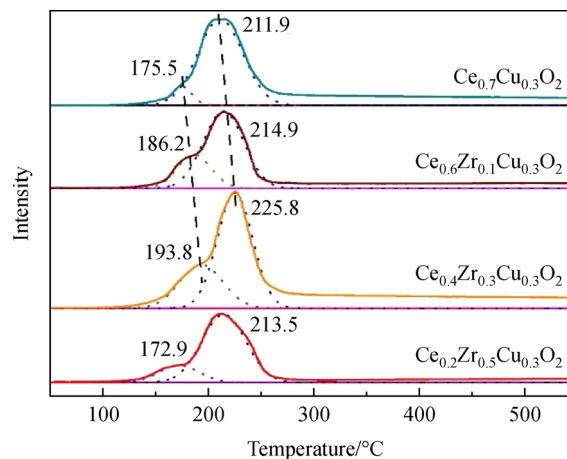


**Fig. 5** H<sub>2</sub>-TPR profiles of the  $\text{Ce}_{0.7-x}\text{Zr}_x\text{Cu}_{0.3}\text{O}_2$  series composites.

interaction with CeO<sub>2</sub>; the latter is due to the reduction of bulk CuO crystals that are weakly associated with CeO<sub>2</sub> [35]. The detailed peak temperatures and hydrogen consumption figures are shown in Table 1.

The shoulder peak showed that hydrogen consumption increased with Zr doping, and reached a maximum at  $x = 0.3$  ( $0.82 \text{ mmol} \cdot \text{g}_{\text{cat}}^{-1}$ ), which showed weak CuO diffraction peaks in the XRD patterns. The low H<sub>2</sub> consumption of  $\text{Ce}_{0.7}\text{Cu}_{0.3}\text{O}_2$  could be because it was not feasible for Cu<sup>2+</sup> ions to enter the CeO<sub>2</sub> framework and the CuO that formed on surface was made of large particles that have weak interaction with CeO<sub>2</sub>.  $\text{Ce}_{0.6}\text{Zr}_{0.1}\text{Cu}_{0.3}\text{O}_2$  also consumed little hydrogen because most of the Cu<sup>2+</sup>

**Table 1** H<sub>2</sub>-TPR and O<sub>2</sub>-TPD data of the Ce<sub>0.7-x</sub>Zr<sub>x</sub>Cu<sub>0.3</sub>O<sub>2</sub> composite oxides

Sample	H <sub>2</sub> -TPR (area/counts)				O <sub>2</sub> -TPD (area/counts)		
	Shoulder peak		Main peak		$\alpha$ peak	$\beta$ peak	$\gamma$ peak
	$T/^\circ\text{C}$	$\text{mmol} \cdot \text{g}_{\text{cat}}^{-1} \text{ a)}$	$T/^\circ\text{C}$	$\text{mmol} \cdot \text{g}_{\text{cat}}^{-1} \text{ a)}$			
$x = 0$	175.5	0.16	211.9	1.99	462.1	56.1	1363.7
$x = 0.1$	186.2	0.49	214.9	1.60	122.4	287.6	1209.4
$x = 0.3$	193.8	0.82	225.8	2.10	199.1	261.8	1810.1
$x = 0.5$	172.9	0.30	213.5	1.56	308.7	130.0	2015.8

a) H<sub>2</sub> consumption calculated from the TPR measurements ( $\text{mmol} \cdot \text{g}_{\text{cat}}^{-1}$ ).

ions entered the CeO<sub>2</sub> lattice, and less CuO formed on the surface. With Ce<sub>0.4</sub>Zr<sub>0.3</sub>Cu<sub>0.3</sub>O<sub>2</sub>, because the surface CuO is made of small particles that have strong interaction with the Ce(Zr)O<sub>2</sub>, it consumed the most hydrogen.

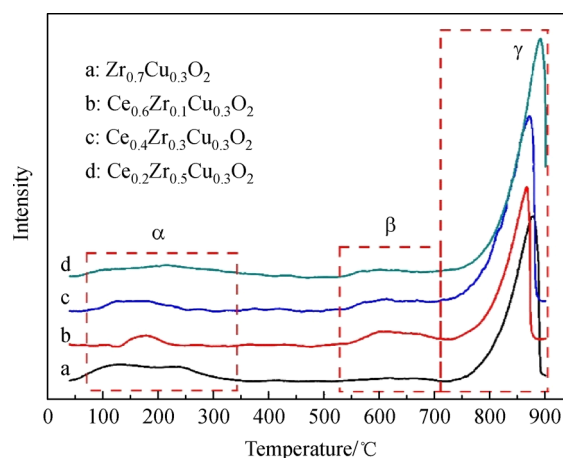
As expected, an increase in the reduction temperature was observed with the Zr doping, e.g., from 175.5 °C for Ce<sub>0.7</sub>Cu<sub>0.3</sub>O<sub>2</sub> to 193.8 °C for Ce<sub>0.4</sub>Zr<sub>0.3</sub>Cu<sub>0.3</sub>O<sub>2</sub>, due to: 1) the larger amounts of hydrogen consumed (e.g., the hydrogen consumption of Ce<sub>0.4</sub>Zr<sub>0.3</sub>Cu<sub>0.3</sub>O<sub>2</sub> is ca. 5 times higher than that of Ce<sub>0.7</sub>Cu<sub>0.3</sub>O<sub>2</sub>, as per Table 1), which delayed the appearance of the reduction peak; 2) the stronger interaction between the copper species and the Ce (Zr)O<sub>2</sub>, which increased the difficulty of the reduction process and increased the reduction temperature.

The strong interaction between CuO and Ce(Zr)O<sub>2</sub> also affected the temperature of the main reduction peak. This is especially prominent in sample  $x = 0.1$ , which consumed less hydrogen, but shows a higher peak temperature (~3 °C) than sample  $x = 0$ . The hydrogen consumption of the main reduction peak increased again for sample  $x = 0.3$ , due to the re-formation of surface CuO.

It is worth noting that the real H<sub>2</sub> consumption value was higher than the theoretical value calculated for complete reduction of Cu<sup>2+</sup> to Cu<sup>0</sup> (e.g., 2.0  $\text{mmol} \cdot \text{g}_{\text{cat}}^{-1}$  for Ce<sub>0.7</sub>Cu<sub>0.3</sub>O<sub>2</sub>). This suggested that, besides the reduction of surface CuO, some active interfacial Ce–O–Cu species were involved in the reduction process (e.g., H<sub>2</sub> + Ce–O–Cu → Ce–□–Cu + H<sub>2</sub>O), as reported elsewhere [36,37]. This is supported by the disappearance of the reduction peak at ~500 °C for CeO<sub>2</sub> [38,39]. Therefore, the reduction of CeO<sub>2</sub> was promoted by the newly formed Ce–O–Cu species, which consumes hydrogen and causes high hydrogen consumption in the reduction process.

The properties of sample  $x = 0.5$  changed significantly compared to that of the other samples, due to the transformation of the matrix structure (from CeO<sub>2</sub> to ZrO<sub>2</sub>). Thus, the peak temperature and the hydrogen consumption for both the shoulder peak and the main peak decreased compared to those of sample  $x = 0.3$ . This provides indirect support for the view that the interfacial Ce–O–Cu species was formed and reduced by H<sub>2</sub> in the Ce-rich samples ( $x \leq 0.3$ ).

Figure 6 shows the O<sub>2</sub>-TPD profile of the Ce<sub>0.7-x</sub>Zr<sub>x</sub>Cu<sub>0.3</sub>O<sub>2</sub>. Three desorption peaks appeared in the profiles,

**Fig. 6** O<sub>2</sub>-TPD profiles of the Ce<sub>0.7-x</sub>Zr<sub>x</sub>Cu<sub>0.3</sub>O<sub>2</sub> composite oxides.

which indicates that the desorption of oxygen occurred mainly in three stages. Based on previous results obtained [12,40], it was inferred that the first peak (70 °C–300 °C) was due to the molecular oxygen that was physically or chemically adsorbed on the surface (e.g., O<sub>2</sub>, O<sub>2</sub><sup>-</sup>, defined as  $\alpha$  oxygen). The second peak (530 °C–700 °C) was due to the atomic oxygen chemically adsorbed on the oxygen vacancies (e.g., O<sup>2-</sup>, O<sup>-</sup>, defined as  $\beta$  oxygen). The third peak (700 °C–900 °C) was due to the oxygen located on the lattice (e.g., O<sup>2-</sup>, defined as  $\gamma$  oxygen). For comparison purposes, we calculated the desorption peak area, which reflects the amount of oxygen desorbed from the sample. The data are listed in Table 1.

For the  $\alpha$  oxygen, the peak area decreased from  $x = 0$  to 0.1, but then increased as more Zr was added. In contrast, the peak area of  $\beta$  oxygen increased initially, but decreased with a further increase in Zr content. The change in peak area could be because of the number of Cu<sup>2+</sup> ions entering the CeO<sub>2</sub> lattice (or the amount of CuO produced on the surface). For example, Ce<sub>0.7</sub>Cu<sub>0.3</sub>O<sub>2</sub> with a higher CuO content released more  $\alpha$  oxygen, and Ce<sub>0.6</sub>Zr<sub>0.1</sub>Cu<sub>0.3</sub>O<sub>2</sub> with a lower CuO content released less  $\alpha$  oxygen. Consequently, we speculated that the molecular oxygen adsorbed on the CuO surface is responsible for the release of  $\alpha$  oxygen.

The  $\beta$  oxygen relates closely to the oxygen vacancy, and

its change could be explained by the number of oxygen vacancies generated in the sample. According to the principle of electroneutrality, we know that when low-valence  $\text{Cu}^{2+}$  enters the  $\text{CeO}_2$  lattice, it can cause the release of atomic oxygen and generate oxygen vacancies. Consequently,  $\text{Ce}_{0.6}\text{Zr}_{0.1}\text{Cu}_{0.3}\text{O}_2$  with more  $\text{Cu}^{2+}$  incorporated shows a larger  $\beta$  desorption peak (or releases more  $\beta$  oxygen). In contrast,  $\text{Ce}_{0.7}\text{Cu}_{0.3}\text{O}_2$  with less  $\text{Cu}^{2+}$  entrance shows a smaller  $\beta$  desorption peak (or releases less  $\beta$  oxygen).

The change in the peak area of the  $\gamma$  oxygen is similar to that of the  $\alpha$  oxygen: with the increase of Zr doping, the peak area first decreased and then increased. This could be related to the Cu–O–Ce bond that formed in the samples. Compared to CuO,  $\text{CeO}_2$  is a better oxygen storage/release material, and the release of lattice oxygen ( $\text{O}_{\text{latt}}$ ) is easier at high temperature. Thus, when more  $\text{Cu}^{2+}$  ions enter the  $\text{CeO}_2$  lattice, the percentage of  $\text{CeO}_2$  decreases and less  $\text{O}_{\text{latt}}$  is released, due to the stronger Cu–O–Ce bonds. This is one reason why  $\text{Ce}_{0.6}\text{Zr}_{0.1}\text{Cu}_{0.3}$  with more  $\text{Cu}^{2+}$

incorporated releases less  $\gamma$  oxygen. Thus, the large  $\gamma$  desorption peak seen with  $\text{Ce}_{0.2}\text{Zr}_{0.5}\text{Cu}_{0.3}\text{O}_2$  could be because: 1) the  $\text{Cu}^{2+}$  ions existed mainly on the surface as CuO and fewer ions entered the  $\text{Ce}(\text{Zr})\text{O}_2$  lattice to form Cu–O–Ce species; 2) the  $\text{CeO}_2$  lattice was distorted with a high level of Zr doping, which facilitates the release of  $\text{O}_{\text{latt}}$ .

Figure 7 presents the XPS spectra of Ce 3d, Zr 3d, Cu 2p and O 1s of the samples. Peak deconvolution of the Ce 3d spectra was performed using a fitting process described in the literature [41]. According to the report of Burroughs et al. [42], the Ce 3d<sub>5/2</sub> and Ce 3d<sub>3/2</sub> signal peaks can be marked as u and v, respectively. The v<sup>1</sup> and u<sup>1</sup> components correspond to the electronic configuration of the  $\text{Ce}^{3+}$  species, that is,  $\text{Ce}^{3+} = (\text{u}^1 + \text{v}^1)$ . From the principle of electroneutrality, we know that the presence of  $\text{Ce}^{3+}$  also indicates the formation of oxygen vacancies in  $\text{CeO}_2$ ; thus the appearance of v<sup>1</sup> and u<sup>1</sup> peaks implies that oxygen vacancies were generated in  $\text{Ce}_{0.7-x}\text{Zr}_x\text{Cu}_{0.3}\text{O}_2$ .

The XPS spectrum of Zr 3d showed that the peak area increased with the increase in Zr doping in the sequence

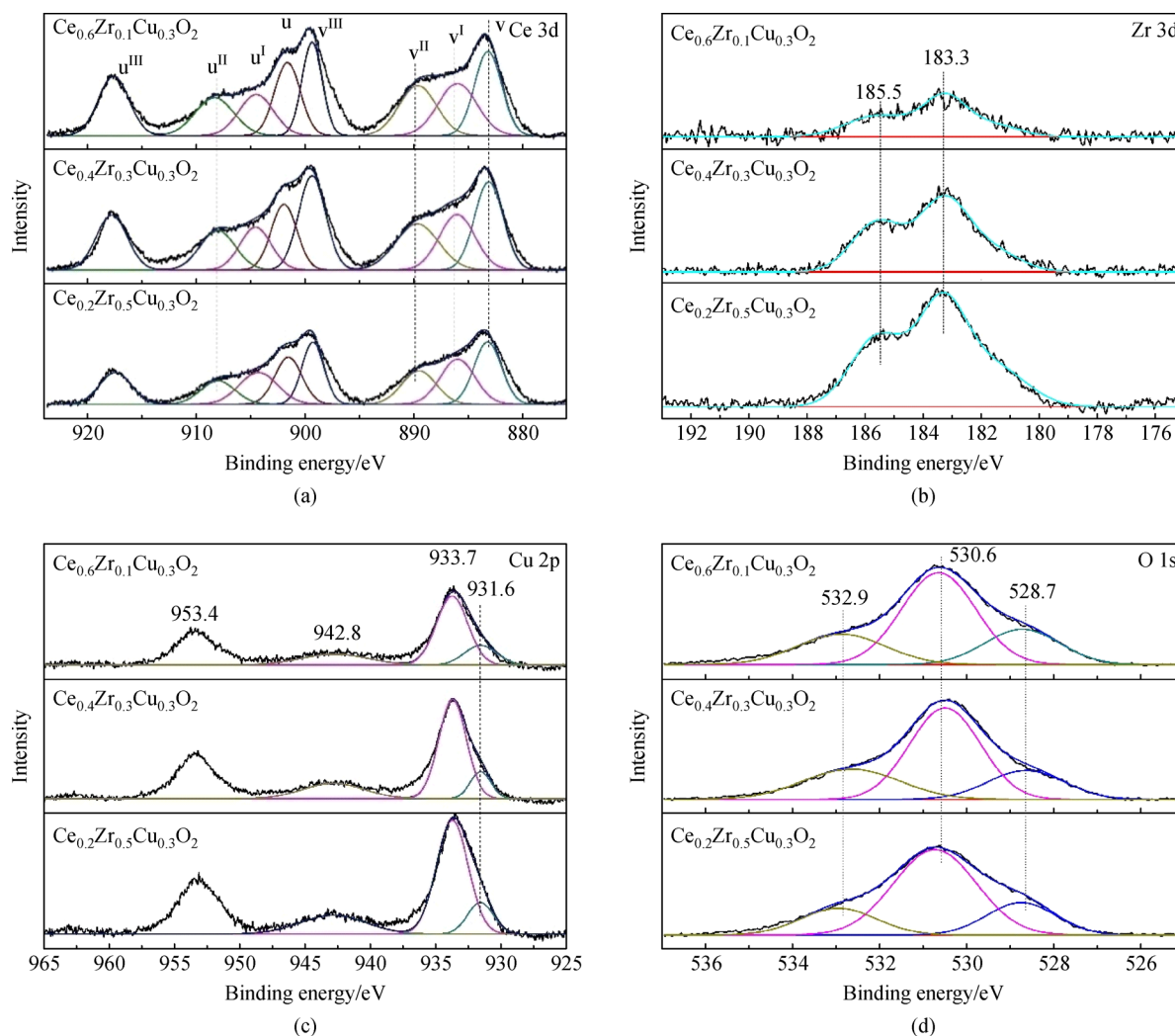


Fig. 7 Ce 3d, Zr 3d, Cu 2p and O 1s fine XPS spectra of the  $\text{Ce}_{0.7-x}\text{Zr}_x\text{Cu}_{0.3}\text{O}_2$  composites.

$\text{Ce}_{0.6}\text{Zr}_{0.1}\text{Cu}_{0.3}\text{O}_2 < \text{Ce}_{0.4}\text{Zr}_{0.3}\text{Cu}_{0.3}\text{O}_2 < \text{Ce}_{0.2}\text{Zr}_{0.5}\text{Cu}_{0.3}\text{O}_2$ . This suggests that the Zr atoms were added to the samples, as desired. According to the literature [43], the peaks at binding energy of 183.3 and 185.5 eV are attributed to Zr 3d<sub>5/2</sub> and Zr 3d<sub>3/2</sub>, respectively, which suggests that the Zr atoms exist as Zr<sup>4+</sup> species. Considering that no segregated CeO<sub>2</sub> or ZrO<sub>2</sub> was observed in the XRD patterns, it was inferred that the Zr atoms entered the CeO<sub>2</sub> framework and formed a Ce(Zr)O<sub>2</sub> solid solution [29].

The Cu 2p<sub>3/2</sub> XPS spectra can be fitted into two peaks, with a main peak at 933.7 eV assigned to the Cu<sup>2+</sup> species, and a weak peak at 931.6 eV assigned to the Cu<sup>+</sup> species. The appearance of the Cu<sup>+</sup> and Ce<sup>3+</sup> species (see above) implies that there is an oxidation-reduction equilibrium in the sample, i.e., Cu<sup>2+</sup> + Ce<sup>3+</sup> ↔ Cu<sup>+</sup> + Ce<sup>4+</sup>. In addition, the distinct satellite peak at 942.8 eV also indicates the presence of the Cu<sup>2+</sup> species. These results indicate that both Cu<sup>2+</sup> and Cu<sup>+</sup> are present in the sample. The peak area of the Cu<sup>2+</sup> species increased with the Zr doping (Table 2), which indicates the formation of more surface CuO crystals, in accordance with the XRD and H<sub>2</sub>-TPR results described above.

**Table 2** Surface atomic copper and oxygen molar ratios obtained from the XPS spectra

Catalysts	Cu <sup>2+</sup> /Cu <sup>+</sup> + Cu <sup>2+</sup>	O <sub>ads</sub> /O <sub>latt</sub> <sup>a)</sup>
Ce <sub>0.6</sub> Zr <sub>0.1</sub> Cu <sub>0.3</sub> O <sub>2</sub>	0.82	2.6
Ce <sub>0.4</sub> Zr <sub>0.3</sub> Cu <sub>0.3</sub> O <sub>2</sub>	0.85	2.9
Ce <sub>0.2</sub> Zr <sub>0.5</sub> Cu <sub>0.3</sub> O <sub>2</sub>	0.87	3.2

a) O<sub>ads</sub>: adsorbed oxygen.

The XPS spectra of O 1s can be fitted into three peaks, which locate at a binding energy of 528.7, 530.6 and 532.9 eV, and correspond to O<sub>latt</sub>, chemically O<sub>ads</sub> on the oxygen vacancies and molecular oxygen adsorbed on the surface or the hydroxyl species, respectively [44]. All samples exhibited a large peak, which was assigned to the O<sub>ads</sub> species. This implies the presence of a large amount of oxygen vacancies. By calculating the molar ratio of O<sub>ads</sub>/O<sub>latt</sub>, we see that the ratio increased with Zr doping, from 2.6 for Ce<sub>0.6</sub>Zr<sub>0.1</sub>Cu<sub>0.3</sub>O<sub>2</sub> to 2.9 for Ce<sub>0.4</sub>Zr<sub>0.3</sub>Cu<sub>0.3</sub>O<sub>2</sub>, and then to 3.2 for Ce<sub>0.1</sub>Zr<sub>0.5</sub>Cu<sub>0.3</sub>O<sub>2</sub> (Table 2). This indicates that Zr doping facilitates the generation of oxygen vacancies. However, considering that Zr and Ce have the same oxidation states (+4) and that the amount of Cu<sup>2+</sup> entering the CeO<sub>2</sub> lattice decreases with the Zr doping, we inferred that the generation of oxygen vacancies is mainly due to distortion of the CeO<sub>2</sub> lattice caused by Zr doping, because of their different ionic radii.

It is noted that the above results were contrary to the change in β oxygen detected in the O<sub>2</sub>-TPD experiment. The reasons for this could be: 1) the XPS technique detects only the oxygen vacancies on the surface, while the O<sub>2</sub>-

TPD results reflect the vacancies in the overall catalyst (both on the surface and in the bulk); 2) at low Zr doping, although more low-valence Cu<sup>2+</sup> cations enter the CeO<sub>2</sub> lattice and generate more oxygen vacancies, they exist mainly in the interior of the sample, rather than on the surface, as Ce and Zr atoms are easier to accumulate on the surface than Cu atoms; 3) the generation of oxygen vacancies by lattice distortion is more feasible than it being caused by Cu<sup>2+</sup> incorporation, as the latter can be partly compensated for by a reduction of Ce<sup>4+</sup> ions (i.e., Ce<sup>4+</sup> → Ce<sup>3+</sup>).

The generation of oxygen vacancy in CeO<sub>2</sub> by Cu and Zr doping was further confirmed by the Raman spectra (Fig. S1, cf. ESM). Two obvious peaks were detected. The strong peak at 465 cm<sup>-1</sup> is related to the symmetric stretching vibration of the Ce–O–Ce bond with the F2g mode; the weak and broad peak at 605 cm<sup>-1</sup> is related to the oxygen vacancy of fluorite CeO<sub>2</sub> [44,45]. From the ratio of the peak area, A<sub>605</sub>/A<sub>465</sub>, we see that the amount of oxygen vacancy in the samples detected by the Raman spectra has the same trend as that detected by the XPS spectra, which verifies the above conclusions.

### 3.3 Catalytic activity for CO oxidation

The effects of Cu content on the catalytic performance of Ce<sub>1-x</sub>Cu<sub>x</sub>O<sub>2</sub> for CO oxidation were first screened, so as to optimize the Cu content. The results showed that CO oxidation activity increases at first, but then decreases with a further increase in Cu content, with the best result obtained at a Ce/Cu molar ratio of 7:3, i.e., Ce<sub>0.7</sub>Cu<sub>0.3</sub>O<sub>2</sub> (Fig. 8(a)). This value was thus selected to prepare the Ce<sub>0.7-x</sub>Zr<sub>x</sub>Cu<sub>0.3</sub>O<sub>2</sub> catalysts for investigation in the following experiments.

The catalytic activity of Ce<sub>0.7-x</sub>Zr<sub>x</sub>Cu<sub>0.3</sub>O<sub>2</sub> for CO oxidation is shown in (Fig. 8(b)). At first, the activity increased rapidly with the Zr doping, but then decreased with a further increase in Zr doping, with the best activity obtained in the range x = 0.1–0.3. The rapid increase in activity from x = 0 to 0.1–0.3 suggests that Zr doping improved the catalytic performance of Cu<sub>0.7</sub>Cu<sub>0.3</sub>O<sub>2</sub> for CO oxidation by increasing the number of oxygen vacancies (for x = 0.1, see O<sub>2</sub>-TPD) or the amount of reducible Cu species (x = 0.3, see H<sub>2</sub>-TPR), which were used for O<sub>2</sub> and CO activation, respectively [46,47]. Although Ce<sub>0.7</sub>Cu<sub>0.3</sub>O<sub>2</sub> has a small β peak area, it also showed good activity for CO oxidation, with 100% CO conversion obtained at 120 °C. This implies that the α oxygen also contributed to the reaction. However, from the overall activity of the samples, it is believed that β oxygen was more reactive than α oxygen for CO oxidation [48,49].

The similar activity of samples x = 0.1 and 0.3 can be explained by the variation in the number of oxygen vacancies and the amount of surface reducible Cu species: sample x = 0.1 has more oxygen vacancies and provides more sites for O<sub>2</sub> adsorption and activation, which

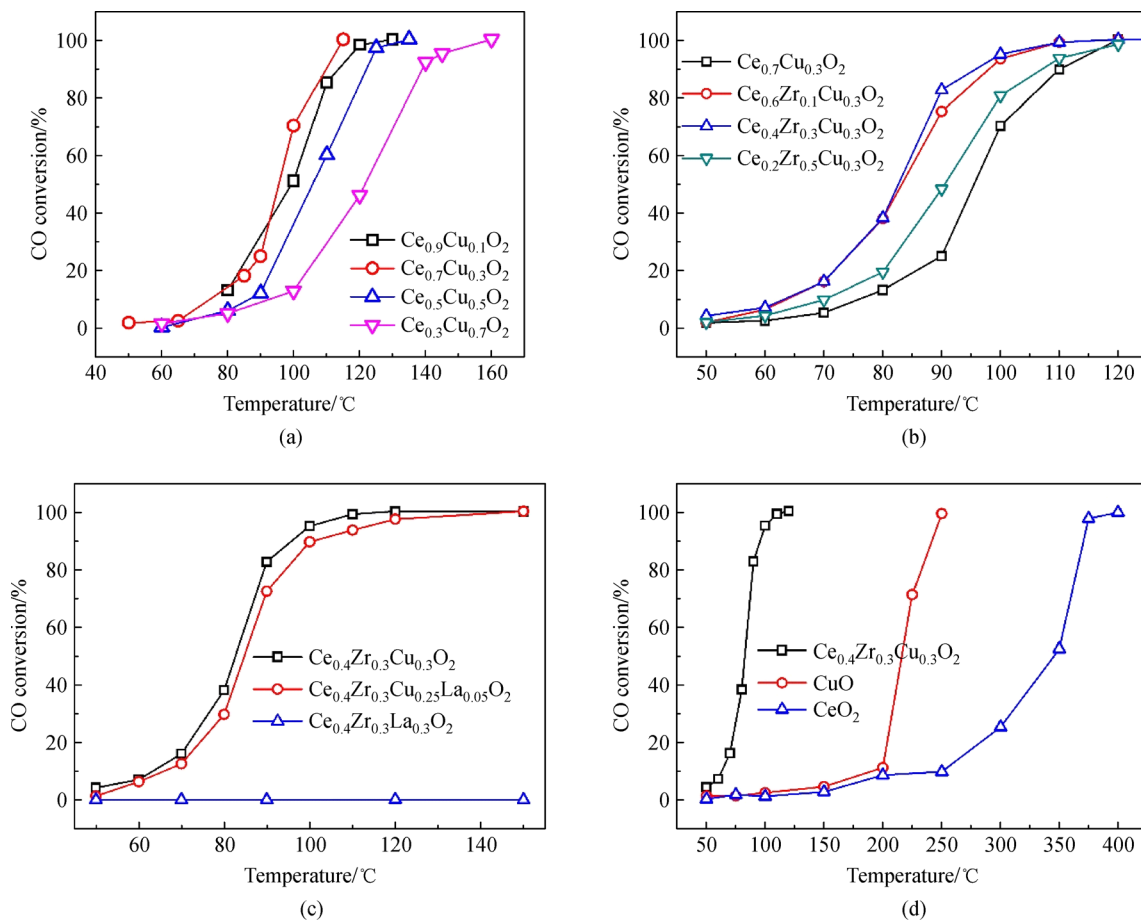


**Fig. 8** CO conversion obtained from the catalysts: (a)  $\text{Ce}_{1-x}\text{Cu}_x\text{O}_2$  composites; (b)  $\text{Ce}_{0.7-x}\text{Zr}_x\text{Cu}_{0.3}\text{O}_2$  composites; (c) La substituted  $\text{Ce}_{0.4}\text{Zr}_{0.3}\text{Cu}_{0.3-y}\text{La}_y\text{O}_2$ ; (d)  $\text{CuO}$ ,  $\text{CeO}_2$  and  $\text{Ce}_{0.4}\text{Zr}_{0.3}\text{Cu}_{0.3}\text{O}_2$ .

facilitates the generation of reactive oxygen atoms; while sample  $x = 0.3$  has more reducible Cu species and offers more sites for CO adsorption and activation, which also favors the reaction proceeding. Therefore, both samples had an advantage in catalyzing the  $\text{CO} + \text{O}_2$  reaction (facilitating either  $\text{O}_2$  activation or CO activation), and showed similar catalytic activities.

The low activity seen with sample  $x = 0.5$  could be because many  $\text{CuO}$  crystals were produced, while few oxygen vacancies were generated on the surface (see the XRD and  $\text{O}_2$ -TPD results), and the  $\text{CuO}$  crystals may have covered some of the oxygen vacancies. Consequently, fewer oxygen vacancies were used for  $\text{O}_2$  adsorption and activation, which means that the supply of O atoms to the reaction was insufficient, and this slowed the reaction rate.

We also investigated the role of Cu species in the reaction, by substituting the Cu atoms with La atoms (Fig. 8(c)). The CO conversions decreased slightly when small amounts of Cu atoms were substituted, i.e.,  $\text{Ce}_{0.4}\text{Zr}_{0.3}\text{Cu}_{0.25}\text{La}_{0.05}\text{O}_2$ , but decreased to almost zero when the Cu atoms were fully replaced with La atoms, i.e.,  $\text{Ce}_{0.4}\text{Zr}_{0.3}\text{La}_{0.3}\text{O}_2$ . This demonstrates that the Cu species plays a crucial role in the reaction. Hence, it is believed that

both the oxygen vacancy and the Cu species are essential for CO oxidation.

The cooperative effects of  $\text{CeO}_2$  and  $\text{CuO}$  were also proved by comparing their activity with that of  $\text{Ce}_{0.4}\text{Zr}_{0.3}\text{Cu}_{0.3}\text{O}_2$  (Fig. 8(d)). A significant increase in activity was observed from  $\text{CeO}_2$  to  $\text{CuO}$  and to  $\text{Ce}_{0.4}\text{Zr}_{0.3}\text{Cu}_{0.3}\text{O}_2$ , which confirms that a cooperative effect was induced between  $\text{CeO}_2$  and  $\text{CuO}$ .  $\text{CeO}_2$  showed the lowest CO oxidation activity, because it has no reducible Cu species, which is used for CO adsorption and activation.  $\text{CuO}$  possessed a certain number of reducible species for CO adsorption and activation, but the lack of oxygen vacancy (a negligible  $\beta$  oxygen desorption peak was observed in the  $\text{O}_2$ -TPD profile) made the activation of oxygen difficult. Hence, it also showed low activity for the reaction.

To further illuminate the importance of oxygen vacancy and Cu species for CO oxidation, two reference catalysts were designed: an etched  $\text{Ce}_{0.4}\text{Zr}_{0.3}\text{Cu}_{0.3}\text{O}_2$  sample that was prepared by etching the  $\text{Ce}_{0.4}\text{Zr}_{0.3}\text{Cu}_{0.3}\text{O}_2$  with  $\text{HNO}_3$ , so as to remove the surface  $\text{CuO}$  crystals; and a  $\text{CuO}/\text{CeO}_2$  sample prepared by depositing  $\text{CuO}$  particles on the surface of  $\text{CeO}_2$  via a two-step process, so as to control the amount of  $\text{Cu}^{2+}$  entering the  $\text{CeO}_2$  lattice, and the

formation of oxygen vacancy (e.g.,  $\text{Cu}^{2+}-\square-\text{Ce}^{4+}$ ). Thus, the former contains interfacial  $\text{Cu}^{2+}-\square-\text{Ce}^{4+}$  species and negligible surface CuO particles, while the latter contains surface CuO particles and negligible  $\text{Cu}^{2+}-\square-\text{Ce}^{4+}$  species. Figure 9 shows that the CO conversion obtained from the three catalysts was in the order: etched  $\text{Ce}_{0.4}\text{Zr}_{0.3}\text{Cu}_{0.3}\text{O}_2 < \text{CuO}/\text{CeO}_2 < \text{Ce}_{0.4}\text{Zr}_{0.3}\text{Cu}_{0.3}\text{O}_2$ . This suggests that CuO is more crucial than  $\text{Cu}^{2+}-\square-\text{Ce}^{4+}$  species for CO oxidation, or in other words, the adsorption and activation of CO is the crucial step of the reaction. However, the co-existence of CuO and Ce- $\square$ -Cu species contributes better to the reaction, due to the cooperative effect induced from them.

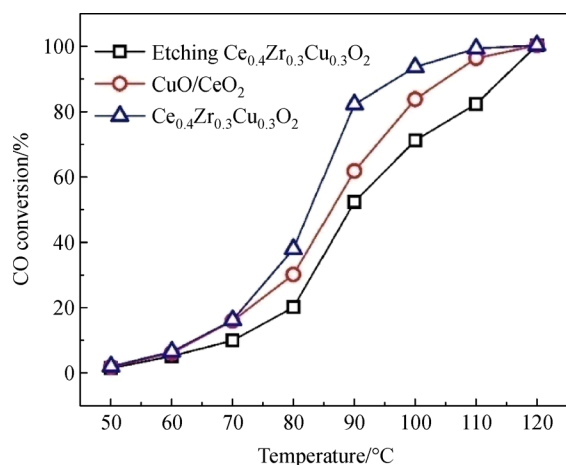
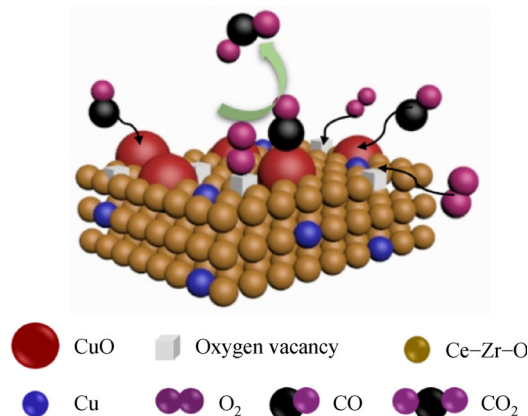


**Fig. 9** Comparison of the activity of  $\text{Ce}_{0.4}\text{Zr}_{0.3}\text{Cu}_{0.3}\text{O}_2$  before and after etching, and of the impregnated  $\text{CuO}/\text{CeO}_2$ .

Consequently, the  $\text{Ce}_{0.4}\text{Zr}_{0.3}\text{Cu}_{0.3}\text{O}_2$  that contains both reducible copper species (e.g., CuO) and oxygen vacancies (e.g.,  $\text{Cu}^{2+}-\square-\text{Ce}^{4+}$ ) showed improved activity for the

reaction, as it provides active sites for both CO and  $\text{O}_2$  adsorption and activation. On this basis, a sketch picture showing the role of CuO and oxygen vacancies in the  $\text{Ce}_{0.7-x}\text{Zr}_x\text{Cu}_{0.3}\text{O}_2$  samples for CO and  $\text{O}_2$  activation was proposed and presented in Scheme 1.



**Scheme 1** Sketch of CO and  $\text{O}_2$  activation and their reaction to form  $\text{CO}_2$  over the  $\text{Ce}_{0.7-x}\text{Zr}_x\text{Cu}_{0.3}\text{O}_2$  composites.

Finally, the long-term stability and water resistance of  $\text{Ce}_{0.4}\text{Zr}_{0.3}\text{Cu}_{0.3}\text{O}_2$  for CO oxidation were investigated, to check the potential for practical applications. Figure 10(a) shows that no appreciable activity loss was observed after running for 30 h, which indicates that the catalyst is stable in the reaction. As for the water resistance, an obvious decrease in the CO conversion was observed when 5%  $\text{H}_2\text{O}$  was added to the reactant gases, while the conversion can be recovered when the water is removed (Fig. 10(b)). This suggests that: the active sites of the catalyst were stable and were not destroyed by water in the reaction; the decrease in CO conversion was because the active sites

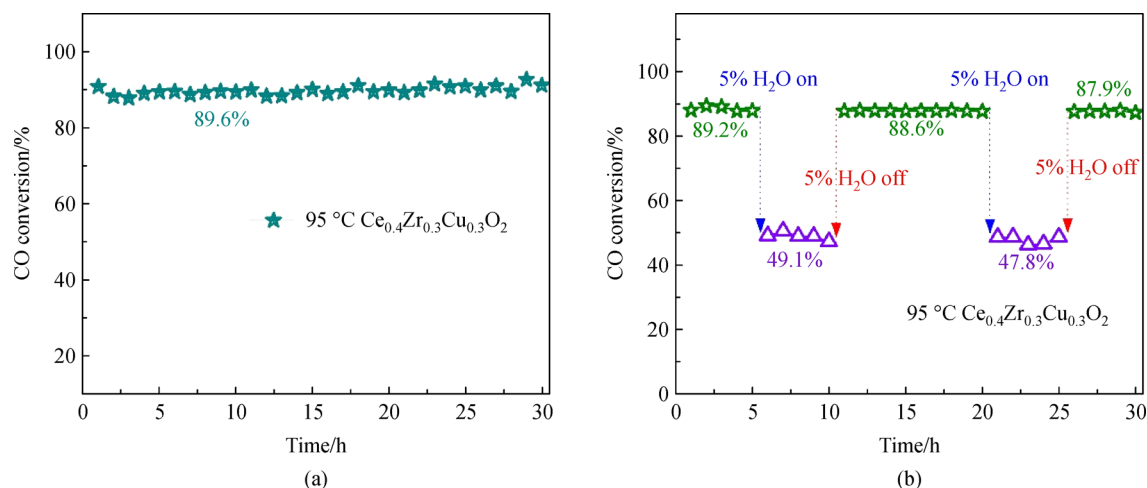


**Fig. 10** (a) Long-term stability of  $\text{Ce}_{0.4}\text{Zr}_{0.3}\text{Cu}_{0.3}\text{O}_2$  for CO oxidation at 95 °C, and (b) the water resistance of  $\text{Ce}_{0.4}\text{Zr}_{0.3}\text{Cu}_{0.3}\text{O}_2$  for CO oxidation at 95 °C (Reaction conditions: using the 0.15 g  $\text{Ce}_{0.4}\text{Zr}_{0.3}\text{Cu}_{0.3}\text{O}_2$  reacted as the catalyst. The reactant (0.8 vol-% CO + 6.0 vol-%  $\text{O}_2$  or 5%  $\text{H}_2\text{O}$ , balanced with Ar) was passed at 60 mL  $\cdot$  min $^{-1}$  flow rate, during which the WHSV is equivalent to 31000 h $^{-1}$ ).

were covered by water, however, this can be refreshed when the water is cut off.

## 4 Conclusions

This work investigated the effect of Zr doping on the catalytic performance of  $\text{Ce}_{0.7-x}\text{Zr}_x\text{Cu}_{0.3}\text{O}_2$  for CO oxidation. It was found that a small amount of Zr doping ( $x \leq 0.1$ ) facilitates  $\text{Cu}^{2+}$  ions entering the  $\text{CeO}_2$  lattice, but excess Zr doping ( $x > 0.1$ ) leads to the formation of surface CuO again and the transformation of the matrix structure (from  $\text{CeO}_2$  to  $\text{ZrO}_2$ ). By correlating the number of reducible Cu species and the oxygen vacancy with the CO oxidation activity, it was inferred that the reducible Cu species was the active site for CO adsorption and activation, and the oxygen vacancy was the active site for  $\text{O}_2$  adsorption and activation. Thus, the  $\text{Ce}_{0.4}\text{Zr}_{0.3}\text{Cu}_{0.3}\text{O}_2$  that contains suitable reducible Cu species and oxygen vacancy showed good activity for CO oxidation, due to the cooperative effect induced between them. The catalyst also has good thermal and hydrothermal stability, and no appreciable activity loss was observed after running for 30 h, but the ability to resist water needs to be improved.

**Acknowledgements** The financial support provided by the following organisations is gratefully acknowledged: the National Natural Science Foundation of China (Grant No. 21976141); the Central Committee Guides Local Science and Technology Development Special Project of Hubei Province (Grant No. 2019ZYD073); the Outstanding Young and Middle-aged Scientific and Technological Innovation Team of the Education Department of Hubei Province (Grant No. T2020011); and the Opening Project of Hubei Key Laboratory of Biomass Fibers and Eco-Dyeing & Finishing (Grant No. STRZ2020003).

**Electronic Supplementary Material** Supplementary material is available in the online version of this article at <https://doi.org/10.1007/s11705-021-2106-2> and is accessible for authorized users.

## References

- Zhang R, Wang J, Zhu X, Liu X, Liu H, Zhou Y, Dong S, La P, Yao J, Liu B. Phase-separated Ce–Co–O catalysts for CO oxidation. *International Journal of Hydrogen Energy*, 2020, 45(23): 12777–12786
- Wang S, Zhang Y, Zhu J, Tang D, Zhao Z, Yang X. Sol-Gel preparation of perovskite oxides using ethylene glycol and alcohol mixture as complexant and its catalytic performances for CO oxidation. *ChemistrySelect*, 2018, 3(43): 12250–12257
- Wang S, Xu X, Zhu J, Tang D, Zhao Z. Effect of preparation method on physicochemical properties and catalytic performances of  $\text{LaCoO}_3$  perovskite for CO oxidation. *Journal of Rare Earths*, 2019, 37(9): 970–977
- Inomata Y, Albrecht K, Yamamoto K. Size-dependent oxidation state and CO oxidation activity of tin oxide clusters. *ACS Catalysis*, 2018, 8(1): 451–456
- Wang S, Xiao P, Xuelian X, Bi H, Liu X, Zhu J. Catalytic CO oxidation and CO + NO reduction conducted on La–Co–O composites: the synergistic effects between  $\text{Co}_3\text{O}_4$  and  $\text{LaCoO}_3$ . *Catalysis Today*, 2020, 376(15): 255–261
- Almana N, Phivilay S P, Laveille P, Hedhili M N, Fornasiero P, Takanabe K, Basset J M. Design of a core-shell Pt– $\text{SiO}_2$  catalyst in a reverse microemulsion system: distinctive kinetics on CO oxidation at low temperature. *Journal of Catalysis*, 2016, 340: 368–375
- Chen S, Zou H, Liu Z, Lin W. DRIFTS study of different gas adsorption for CO selective oxidation on Cu–Zr–Ce–O catalysts. *Applied Surface Science*, 2009, 255(15): 6963–6967
- Ye Q, Wang J, Zhao J, Yan L, Cheng S, Kang T, Dai H. Pt or Pd-doped Au/ $\text{SnO}_2$  catalysts: high activity for low-temperature CO oxidation. *Catalysis Letters*, 2010, 138(1): 56–61
- Chen S F, Li J P, Qian K, Xu W P, Lu Y, Huang W X, Yu S H. Large scale photochemical synthesis of M@ $\text{TiO}_2$  nanocomposites (M = Ag, Pd, Au, Pt) and their optical properties, CO oxidation performance, and antibacterial effect. *Nano Research*, 2010, 3(4): 244–255
- Li N, Chen Q Y, Luo L F, Huang W X, Luo M F, Hu G S, Lu J Q. Kinetic study and the effect of particle size on low temperature CO oxidation over Pt/ $\text{TiO}_2$  catalysts. *Applied Catalysis B: Environmental*, 2013, 142–143: 523–532
- Renuka N K, Anas K, Aniz C U. Synthesis, characterisation and activity of SBA-16 supported oxidation catalysts for CO conversion. *Chinese Journal of Catalysis*, 2015, 36(8): 1237–1241
- Kang R, Wei X, Bin F, Wang Z, Qinglan H, Dou B. Reaction mechanism and kinetics of CO oxidation over a  $\text{CuO}/\text{Ce}_{0.75}\text{Zr}_{0.25}\text{O}_{2-\delta}$  catalyst. *Applied Catalysis A, General*, 2018, 565(5): 46–58
- Atzori L, Cutrufello M G, Meloni D, Onida B, Gazzoli D, Ardu A, Monaci R, Sini M F, Rombi E. Characterization and catalytic activity of soft-templated NiO– $\text{CeO}_2$  mixed oxides for CO and  $\text{CO}_2$  co-methanation. *Frontiers of Chemical Science and Engineering*, 2021, 15(2): 251–268
- Li R, Yang Y, Sun N, Kuai L. Mesoporous Cu–Ce– $\text{O}_x$  solid solutions from spray pyrolysis for superior low-temperature CO oxidation. *Chemistry (Weinheim an der Bergstrasse, Germany)*, 2019, 25(68): 15586–15593
- Desyatykh I V, Vedyagin A A, Mishakov I V, Shubin Y V. CO oxidation over fibreglasses with doped Cu–Ce–O catalytic layer prepared by surface combustion synthesis. *Applied Surface Science*, 2015, 349: 21–26
- AlKetbi M, Polychronopoulou K, Abi Jaoude M, Vasiliades M A, Sebastian V, Hinder S J, Baker M A, Zedan A F, Efstathiou A M. Cu–Ce–La– $\text{O}_x$  as efficient CO oxidation catalysts: effect of Cu content. *Applied Surface Science*, 2020, 505: 144474
- Zhang X, Wang H, Wang Z, Qu Z. Adsorption and surface reaction pathway of  $\text{NH}_3$  selective catalytic oxidation over different Cu–Ce–Zr catalysts. *Applied Surface Science*, 2018, 447: 40–48
- Baneshi J, Haghighi M, Jodeiri N, Abdollahifar M, Ajamein H. Urea-nitrate combustion synthesis of  $\text{ZrO}_2$  and  $\text{CeO}_2$  doped  $\text{CuO}/\text{Al}_2\text{O}_3$  nanocatalyst used in steam reforming of biomethanol for hydrogen production. *Ceramics International*, 2014, 40(9, Part A): 14177–14184

19. Han Y, Wang Y, Ma T, Li W, Zhang J, Zhang M. Mechanistic understanding of Cu-based bimetallic catalysts. *Frontiers of Chemical Science and Engineering*, 2020, 14(5): 689–748
20. Yu W, Zhou Q, Wang H, Liu Y, Chu W, Cai R, Yang W. Selective removal of CO from hydrocarbon-rich industrial off-gases over CeO<sub>2</sub>-supported metal oxides. *Journal of Materials Science*, 2020, 55(6): 2321–2332
21. Liu X, Jia S, Yang M, Tang Y, Wen Y, Chu S, Wang J, Shan B, Chen R. Activation of subnanometric Pt on Cu-modified CeO<sub>2</sub> via redox-coupled atomic layer deposition for CO oxidation. *Nature Communications*, 2020, 11(1): 4240
22. Cabello A P, Ulla M A, Zamaro J M. CeO<sub>2</sub>/CuO<sub>x</sub> nanostructured films for CO oxidation and CO oxidation in hydrogen-rich streams using a micro-structured reactor. *Topics in Catalysis*, 2019, 62(12): 931–940
23. Pati R K, Lee I C, Hou S, Akhuemonkhan O, Gaskell K J, Wang Q, Frenkel A I, Chu D, Salamanca-Riba L G, Ehrman S H. Flame synthesis of nanosized Cu–Ce–O, Ni–Ce–O, and Fe–Ce–O catalysts for the water-gas shift (WGS) reaction. *ACS Applied Materials & Interfaces*, 2009, 1(11): 2624–2635
24. Li S, Hao Q, Zhao R, Liu D, Duan H, Dou B. Highly efficient catalytic removal of ethyl acetate over Ce/Zr promoted copper/ZSM-5 catalysts. *Chemical Engineering Journal*, 2016, 285: 536–543
25. Li K, Lyu T, He J, Jang B W L. Selective hydrogenation of acetylene over Pd/CeO<sub>2</sub>. *Frontiers of Chemical Science and Engineering*, 2020, 14(6): 929–936
26. Vidal H, Kašpar J, Pijolat M, Colón G, Bernal S, Cordón A, Perrichon V, Fally F. Redox behavior of CeO<sub>2</sub>–ZrO<sub>2</sub> mixed oxides. *Applied Catalysis B: Environmental*, 2000, 27(1): 49–63
27. Martínez-Arias A, Fernández-García M, Gálvez O, Coronado J M, Anderson J A, Conesa J C, Soria J, Munuera G. Comparative study on redox properties and catalytic behavior for CO oxidation of CuO/CeO<sub>2</sub> and CuO/ZrCeO<sub>4</sub> catalysts. *Journal of Catalysis*, 2000, 195(1): 207–216
28. Vikanova K, Redina E, Kapustin G, Nissenbaum V, Mishin I, Kostyukhin E, Kustov L. Template-free one-step synthesis of micro-mesoporous CeO<sub>2</sub>–ZrO<sub>2</sub> mixed oxides with a high surface area for selective hydrogenation. *Ceramics International*, 2020, 46(9): 13980–13988
29. Shang H, Zhang X, Xu J, Han Y. Effects of preparation methods on the activity of CuO/CeO<sub>2</sub> catalysts for CO oxidation. *Frontiers of Chemical Science and Engineering*, 2017, 11(4): 603–612
30. Qi L, Yu Q, Dai Y, Tang C, Liu L, Zhang H, Gao F, Dong L, Chen Y. Influence of cerium precursors on the structure and reducibility of mesoporous CuO–CeO<sub>2</sub> catalysts for CO oxidation. *Applied Catalysis B: Environmental*, 2012, 119–120: 308–320
31. Cecilia J A, Arango-Díaz A, Rico-Pérez V, Bueno-López A, Rodríguez-Castellón E. The influence of promoters (Zr, La, Tb, Pr) on the catalytic performance of CuO–CeO<sub>2</sub> systems for the preferential oxidation of CO in the presence of CO<sub>2</sub> and H<sub>2</sub>O. *Catalysis Today*, 2015, 253: 115–125
32. Reyes-Carmona Á, Arango-Díaz A, Moretti E, Talon A, Storaro L, Lenarda M, Jiménez-López A, Rodríguez-Castellón E. CuO/CeO<sub>2</sub> supported on Zr doped SBA-15 as catalysts for preferential CO oxidation (CO-PROX). *Journal of Power Sources*, 2011, 196(9): 4382–4387
33. Manzoli M, Monte R D, Boccuzzi F, Coluccia S, Kašpar J. CO oxidation over CuO<sub>x</sub>–CeO<sub>2</sub>–ZrO<sub>2</sub> catalysts: transient behaviour and role of copper clusters in contact with ceria. *Applied Catalysis B: Environmental*, 2005, 61(3): 192–205
34. Chiou J Y Z, Lai C L, Yu S W, Huang H H, Chuang C L, Wang C B. Effect of Co, Fe and Rh addition on coke deposition over Ni/Ce<sub>0.5</sub>Zr<sub>0.5</sub>O<sub>2</sub> catalysts for steam reforming of ethanol. *International Journal of Hydrogen Energy*, 2014, 39(35): 20689–20699
35. Wang Y, Zheng Y, Wang Y, Li K, Wang Y, Jiang L, Zhu X, Wei Y, Wang H. Syngas production modified by oxygen vacancies over CeO<sub>2</sub>–ZrO<sub>2</sub>–CuO oxygen carrier via chemical looping reforming of methane. *Applied Surface Science*, 2019, 481: 151–160
36. Zhao Y, Chen K, Zou Q, Fang J, Zhu S, He S, Lu J, Luo Y. Insights into the essential roles of tin and chloride species within Cu–CeO<sub>2</sub> based catalysts for CO preferential oxidation in H<sub>2</sub>-rich stream. *Journal of Power Sources*, 2021, 484: 229181
37. Bo L, Sun S. Microwave-assisted catalytic oxidation of gaseous toluene with a Cu–Mn–Ce/cordierite honeycomb catalyst. *Frontiers of Chemical Science and Engineering*, 2019, 13(2): 385–392
38. Ayastuy J L, Gurbani A, González-Marcos M P, Gutiérrez-Ortiz M A. Selective CO oxidation in H<sub>2</sub> streams on CuO/Ce<sub>x</sub>Zr<sub>1-x</sub>O<sub>2</sub> catalysts: correlation between activity and low temperature reducibility. *International Journal of Hydrogen Energy*, 2012, 37(2): 1993–2006
39. Bera P, Hornés A, Cámara A L, Martínez Arias A. DRIFTS-MS studies of preferential oxidation of CO in H<sub>2</sub> rich stream over (CuO)<sub>0.7</sub>(CeO<sub>2</sub>)<sub>0.3</sub> and (Cu<sub>0.9</sub>Mn<sub>0.1</sub>O)<sub>0.7</sub>(CeO<sub>2</sub>)<sub>0.3</sub> (M = Co, Zn and Sn) catalysts. *Catalysis Today*, 2010, 155(3): 184–191
40. Yao H C, Yao Y F Y. Ceria in automotive exhaust catalysts: I. Oxygen storage. *Journal of Catalysis*, 1984, 86(2): 254–265
41. Kang R, Wei X, Bin F, Wang Z, Hao Q, Dou B. Reaction mechanism and kinetics of CO oxidation over a CuO/Ce<sub>0.75</sub>Zr<sub>0.25</sub>O<sub>2-δ</sub> catalyst. *Applied Catalysis A, General*, 2018, 565: 46–58
42. Burroughs P, Hamnett A, Orchard A F, Thornton G. Satellite structure in the X-ray photoelectron spectra of some binary and mixed oxides of lanthanum and cerium. *Journal of the Chemical Society, Dalton Transactions: Inorganic Chemistry*, 1976, 17: 1686–1698
43. Luo M F, Zheng X M, Laitinen R, Ugalde M, Román P, Lezama L, Rojo T. Redox behaviour of CeO<sub>2</sub> and Ce<sub>0.5</sub>Zr<sub>0.5</sub>O<sub>2</sub> supported CuO catalysts for CO oxidation. *Acta Chemica Scandinavica. Series A: Physical and Inorganic Chemistry*, 1998, 52: 1183–1187
44. Liu C, Xian H, Jiang Z, Wang L, Zhang J, Zheng L, Tan Y, Li X. Insight into the improvement effect of the Ce doping into the SnO<sub>2</sub> catalyst for the catalytic combustion of methane. *Applied Catalysis B: Environmental*, 2015, 176–177: 542–552
45. Liu L, Yao Z, Liu B, Dong L. Correlation of structural characteristics with catalytic performance of CuO/Ce<sub>x</sub>Zr<sub>1-x</sub>O<sub>2</sub> catalysts for NO reduction by CO. *Journal of Catalysis*, 2010, 275(1): 45–60
46. Chen A, Yu X, Zhou Y, Miao S, Li Y, Kuld S, Sehested J, Liu J, Aoki T, Hong S, et al. Structure of the catalytically active copper-ceria interfacial perimeter. *Nature Catalysis*, 2019, 2(4): 334–341
47. Tang X, Zhang B, Li Y, Xu Y, Xin Q, Shen W. CuO/CeO<sub>2</sub> catalysts:

- redox features and catalytic behaviors. *Applied Catalysis A, General*, 2005, 288(1): 116–125
48. Liu X, Wang K, Zhou Y, Tang X, Zhu X, Zhang R, Zhang X, Jiang X, Liu B. *In-situ* fabrication of noble metal modified (Ce, Zr)O<sub>2-δ</sub> monolithic catalysts for CO oxidation. *Applied Surface Science*, 2019, 483(31): 721–729
49. Liu X, Wang K, Zhou Y, Zhang X, Tang X, Ren P, Jiang X, Liu B. *In-situ* fabrication of Ce-rich CeO<sub>2</sub> nanocatalyst for efficient CO oxidation. *Journal of Alloys and Compounds*, 2019, 792(5): 644–651